RSC Advances

PAPER

View Article Online
View Journal | View Issue

Cite this: *RSC Adv.*, 2026, **16**, 12080

Investigating the catalytic and antimicrobial properties of ternary cesium/polyethylene glycol-SrO supported by molecular docking and DFT analysis

Misbah Tariq,[a] Muhammad Imran,[b] Ali Haider,[c] Iram Shahzadi,[d] Fatima Javed,[e] Anwar Ul-Hamid,[f] Norah A. Albassami,[g] Ghazanfar Nazir[h] and Muhammad Ikram *[e]

Received 31st January 2026
Accepted 17th February 2026

DOI: 10.1039/d6ra00841k

rsc.li/rsc-advances

This study explores the use of ternary system nanocomposites to degrade methyl orange (MO) dye in water as well as assesses their antibacterial properties. For this purpose, the co-precipitation process was adopted to synthesize strontium oxide (SrO) doped with a fixed amount (3 wt%) of polyethylene glycol (PEG) as a capping agent, and various weight ratios (2 and 4 wt%) of cesium (Cs) were added to the binary system (PEG-SrO). Advanced characterization techniques were employed to analyze the various properties of the resulting materials. XRD unveiled the cubic crystal structure of SrO, while TEM revealed randomly oriented nanorods in the pristine sample. The optimum sample (2% Cs/PEG-SrO) demonstrated efficient catalytic activity (CA) in degrading MO dye. The 4% Cs/PEG-SrO sample showed significant bactericidal efficacy against *Escherichia coli* (*E. coli*), exhibiting inhibition zones ranging from 2.05 to 6.15 mm at higher concentrations. Furthermore, the computational findings align with the experimental data, offering strong evidence for the microbial effectiveness of Cs/PEG-SrO in hindering DNA gyrase in *E. coli*.

1. Introduction

As industries evolve and populations grow, the sources of pollution have surged immensely. A key factor influencing this issue is the extensive use of colorants across multiple sectors, especially textiles, food, and pharmaceuticals.[1] In the textile industry, processing inefficiencies in dyeing lead to substantial losses and discharge of dyestuffs into water bodies, ultimately causing environmental pollution.[2] Azo dyes are classified as the most significant and extensive category of synthetic organic dyes, attributed to their non-biodegradability and chemical stability.[3] MO is an organic azo dye known for its high toxicity and widespread applications in various industries, including food, leather, textile, and paper industries. However, its release into the ecosystem poses significant risks to human health and presents a considerable threat to other living organisms.[4] Mastitis is recognized as a highly prevalent disease affecting dairy cattle globally. Various infectious agents, including fungi, bacteria, and mycoplasma, have been associated with mastitis; however, bacteria are the primary factor in its occurrence. Environmental mastitis is often caused by *E. coli*, leading to inflammation symptoms including high fever, decreased milk production, and toxemia.[5,6] There are many approaches for treating or decolorizing MO dye, including adsorption, photocatalytic degradation, coagulation, catalysis, and nanofiltration.[7–9] Among these methods, catalysis is a crucial and widely utilized technique owing to its environmentally friendly nature, cost-effectiveness, and energy efficiency.[10] Among the metal oxides (MOs), including Al_2O_3, CuO, MgO, SrO, and CaO, SrO has garnered significant interest owing to its basic nature and exceptional optical, catalytic, and antibacterial properties.[11–13] However, it has some limitations, including a small surface area and a high recombination rate of charge carriers, constraining its application in degradation.[12,14] The

[a]*Department of Chemistry, Government College University, Faisalabad, Pakpattan Road, Sahiwal, Punjab, 57000, Pakistan*
[b]*Interdisciplinary Research Center for Hydrogen Technologies and Carbon Management, King Fahd University of Petroleum and Minerals, Dhahran, 31261, Saudi Arabia*
[c]*Department of Clinical Sciences, Faculty of Veterinary and Animal Sciences, Muhammad Nawaz Shareef, University of Agriculture, Multan 66000, Punjab, Pakistan*
[d]*School of Pharmacy, University of Management and Technology, Lahore 54770, Pakistan*
[e]*Solar Cell Applications Research Lab, Department of Physics, Government College University Lahore, Lahore 54000, Punjab, Pakistan. E-mail: dr.muhammadikram@gcu.edu.pk*
[f]*Core Research Facilities, Research Institute, King Fahd University of Petroleum & Minerals, Dhahran 31261, Saudi Arabia*
[g]*Chemistry Department, Faculty of Science, King Khalid University, P.O. Box 9004, Abha 61413, Saudi Arabia*
[h]*Department of Nanotechnology and Advanced Materials Engineering, Hybrid Materials Research Center (HMC), Sejong University, Seoul, 05006, Republic of Korea*

incorporation of PEG as a dopant could potentially improve the surface area of nanostructures (NSs) and subsequently enhance their CA.[15] Moreover, PEG carriers are known as a promising alternative for effective drug delivery in pharmaceutical applications owing to their stability, enhancement of drug solubility, and biocompatibility.[16] Nevertheless, challenges related to high recombination rates and surface modifications persist. The introduction of Cs as a dopant has the potential to reduce the recombination rate of e^-/h^+ pairs, promote the induction of more active sites, and cause alterations in the electronic structure of samples.[17]

Herein, SrO, PEG-SrO, and Cs/PEG-SrO (2 and 4 wt%) were synthesized using the co-precipitation method. Different characterization techniques were performed to study the structural, optical, and morphological properties of synthesized samples. Following this, the effectiveness of the nanomaterials in degrading MO dye and their antimicrobial properties against *E. coli* were investigated, along with molecular docking and DFT analysis.

2. Experimental work

2.1. Materials

$SrCl_2 \cdot 6H_2O$ (99%), cesium nitrate ($CsNO_3$, 99%), and NaOH (>98%) were obtained from Sigma Aldrich, Germany. Polyethylene glycol (PEG) was purchased from Fluka Chemie (Switzerland).

2.2. Synthesis of pristine and doped SrO

The coprecipitation method was employed to synthesize SrO as our previous study with few characterization reused[11] (sample 1), 0.5 M $SrCl_2 \cdot 6H_2O$ was vigorously stirred at 80 °C for 2 h, as depicted in Fig. 1. To obtain precipitates and sustain a pH of ~12, a sufficient quantity of NaOH was carefully added into the colloidal solution. After that, the precipitates were subjected to centrifugation twice with deionized (DI) water and ethanol at 7000 rpm for 7 min. The resulting sediments were subsequently dried overnight at 120 °C and ground to achieve a nano powder of SrO. For sample 2 (PEG-SrO), PEG was added to the $SrCl_2 \cdot 6H_2O$ solution under the aforementioned conditions. To form a ternary system (2 and 4 wt% Cs-doped PEG-SrO), $CsNO_3$ was incorporated as a source of Cs into the precursor solution of sample 2 under the same conditions (samples 3 and 4, respectively).

2.3. Catalysis

The CA of the SrO and doped samples was evaluated against MO dye. To preserve the purity of the experiment, all reagents, such as MO (oxidizing dye) and $NaBH_4$ (reducing agent), were used

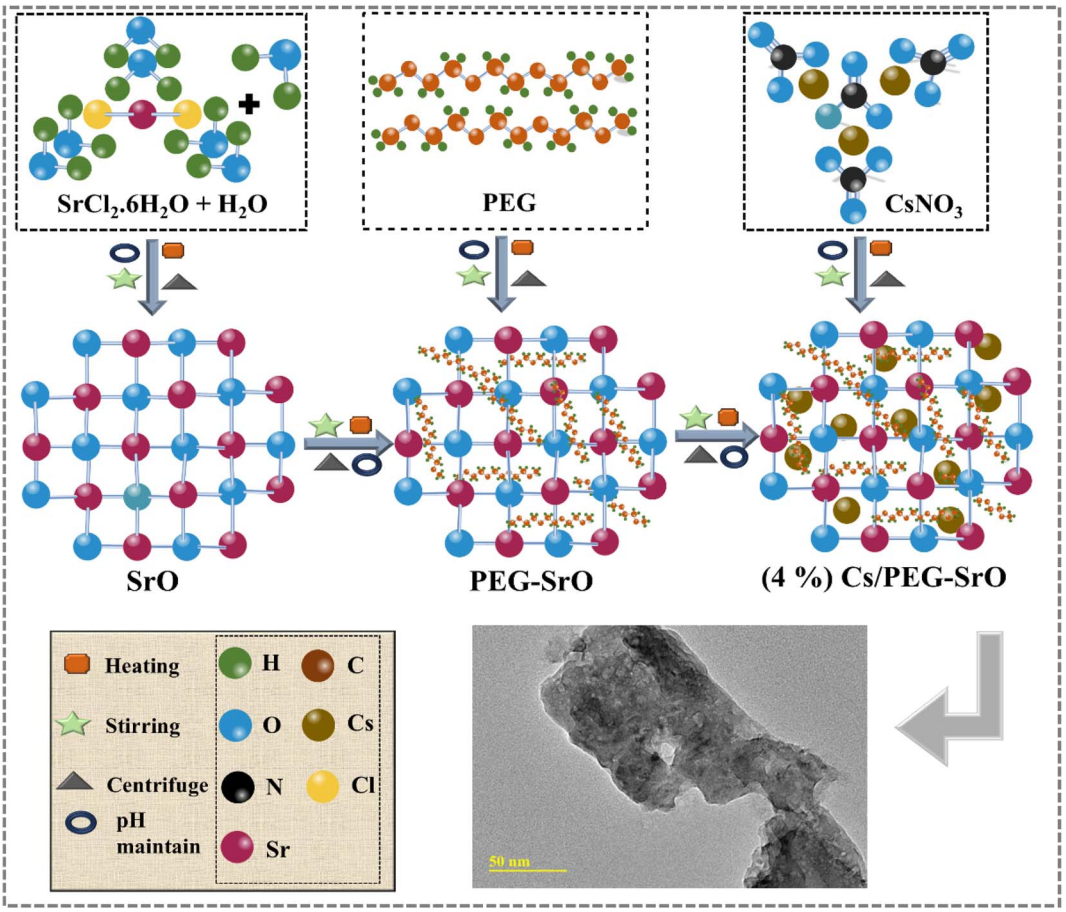

Fig. 1 Schematic of the preparation of SrO, PEG-SrO, and (2 and 4 wt%) Cs/PEG-SrO.

promptly upon preparation. Firstly, 3 mL of MO was added to 400 μL of $NaBH_4$ solution in the absence of light, and then 400 μL of the synthesized material was introduced to evaluate the degradation efficiency. The performance was assessed under basic, acidic, and neutral conditions, where NaOH and H_2SO_4 were utilized to adjust the pH of the solution. Absorption reactions were monitored using a UV-vis spectrometer at ambient temperature within the wavelength range of 200 to 800 nm. The presence of $NaBH_4$ and catalysts led to the transformation of the MO dye into its colorless form, exhibiting efficient dye degradation. The following equation was used to calculate the dye degradation percentage by each sample (eqn (1)).

$$\% \text{ Degradation} = (C_0 - C_t)/C_0 \times 100 \quad (1)$$

where C_0 represents the initial concentration at t_0 and C_t is the final concentration at t.

2.3.1. Isolation and identification of MDR *E. coli*. Unprocessed milk samples from lactating cows were accumulated into sterilized glassware by direct milking. The cows were selected from various farms, veterinary clinics, and marketplaces located across the Punjab province of Pakistan. After acquiring the samples, the milk was instantly transported to the laboratory at 4 °C. Coliforms present in unpasteurized milk were enumerated on MacConkey Agar (MA), with all agar plates incubated at 37 °C for a duration of 48 h.

E.coli was preliminarily identified *via* colonial morphology using biochemical testing and Gram stain technology by adhering to the steps detailed in Bergey's Manual of Determinative Bacteriology (BMDB).[18]

2.3.2. Antibiotic susceptibility. The disk diffusion approach reported by Baeur *et al.*[19] was utilized to evaluate antibiotic susceptibility employing Mueller-Hinton agar (MHA). By applying the test, the antibiotic resistance of the bacteria was determined against certain antibiotics (classes) such as ceftriaxone (Cro) 30 μg (cephalosporins), imipenem (Imi) 10 μg (carbapenem), azithromycin (Azm) 15 μg (macrolides), ciprofloxacin (Cip) 5 μg (quinolones), amoxycillin (A) 30 μg (penicillins), gentamicin (Gm) 10 μg (aminoglycosides), and tetracycline (Te) 30 μg (tetracyclines).[20] The purified *E. coli* bacteria cultures were cultivated with a turbidity adjusted to 0.5 MacFarland. After that, they were spread-plated over Muller-Hinton Agar (MHA). To prevent the overlapping of inhibition zones, the antibiotic disks were placed at a distance from each other on the surface of the inoculated plate. At 37 °C, each plate was incubated for 24 h, and the interpretation of the outcomes was done in accordance with Clinical and Laboratory Standards Institute.[21] MDR bacterium showed resistance to at least three antibiotics.[22]

2.3.3. Antibacterial evaluation. The agar well diffusion method was used to assess the *in vitro* antimicrobial action potential of pure and doped SrO on isolated MDR *E. coli* obtained from mastitis milk. The bacterial samples were collected using swabs and then inoculated onto Petri dishes filled with MacConkey agar at a concentration of 1.5 × 108 CFU mL^{-1}. A sterile cork borer was used to create 6 mm diameter wells. Different concentrations of pure and doped samples ranging from (0.5 mg/50 μL) to (1.0 mg/50 μL) were applied. DI water and ciprofloxacin (0.005 mg/50 μL) were used as negative and positive controls, respectively.[23,24]

2.3.4. Statistical analysis. The efficacy of antimicrobial activity, particularly regarding inhibition zone size (mm), was assessed *via* statistical analysis utilizing one-way analysis of variance (ANOVA) with SPSS 20.[25]

2.4. Structure preparation and docking studies

Sybyl-X 2.0/SKETCH established the three-dimensional framework of Cs/PEG-SrO, subsequently optimizing its energy through the Tripos force field and Gasteiger Hückel atomic charges, resulting in a conformation that enhances biological activity.[26] The enhancement of protein structures was achieved through structural preparation methodologies within the SYBYL-X 2.0 module, encompassing the incorporation of absent hydrogen atoms and assignment of electrical charges. Following 1000 cycles, the energy reduction process yielded a convergence gradient of 0.05 kcal mol^{-1} through the Powell technique. The target protein crystal structure with PDB ID: 5MMN (Chain A) was positioned using the Surflex–Dock module of the SYBYL-X 2.0 software.[27] The crystallographic water molecules were removed and absent hydrogen atoms and electrical charges were added prior to docking. The binding site based on the co-crystallized ligand present in the 5MMN structure was employed to establish the docking grid. The docking protocol was subjected to validation through extraction of the native crystallographic ligand, which was subsequently re-docked into an identical binding pocket. The reproduced binding pose exhibited robust alignment with the original crystal orientation, affirming the dependability of docking parameters. Subsequently, PEG-SrO, Cs/PEG-SrO, and ciprofloxacin were subjected to docking within the validated binding site. Ciprofloxacin functioned as the reference ligand, affirming the credibility of the docking model. Ten docking poses were generated for each ligand to assess the conformational space of the binding site. Subsequently, assessment of the binding interactions with the corresponding targets was conducted, employing the Hammerhead scoring technique to evaluate these potential ligand conformations.

3. Results and discussion

The phase identification and crystal plane structure of SrO, PEG-SrO, and (2 and 4 wt%) Cs/PEG-SrO were investigated using XRD in the 2θ range of 15° to 70° (Fig. 2a). The diffraction peaks located at 25.17° (202), 35.9° (310), 38.9° (312), 40.17° (111), 47.07° (240), and 50.16° (220) are ascribed to the cubic structure of SrO (JCPDS no. 01-075-0263).[28,29] The two peaks located at 31.55° (111), and 62.82° (311) are related to tetragonal SrO (JCPDS card no. 00-027-1304). The single peak at 23.04° (201) is assigned to the orthorhombic geometry of Sr_4O_8 (JCPDS card no. 96-900-8162). Meanwhile, the diffraction peaks at 28.23°, 58.39°, and 64.5° corresponded to the (020), (040), and (331) planes, confirming the tetragonal structure of Sr_1O_{10},

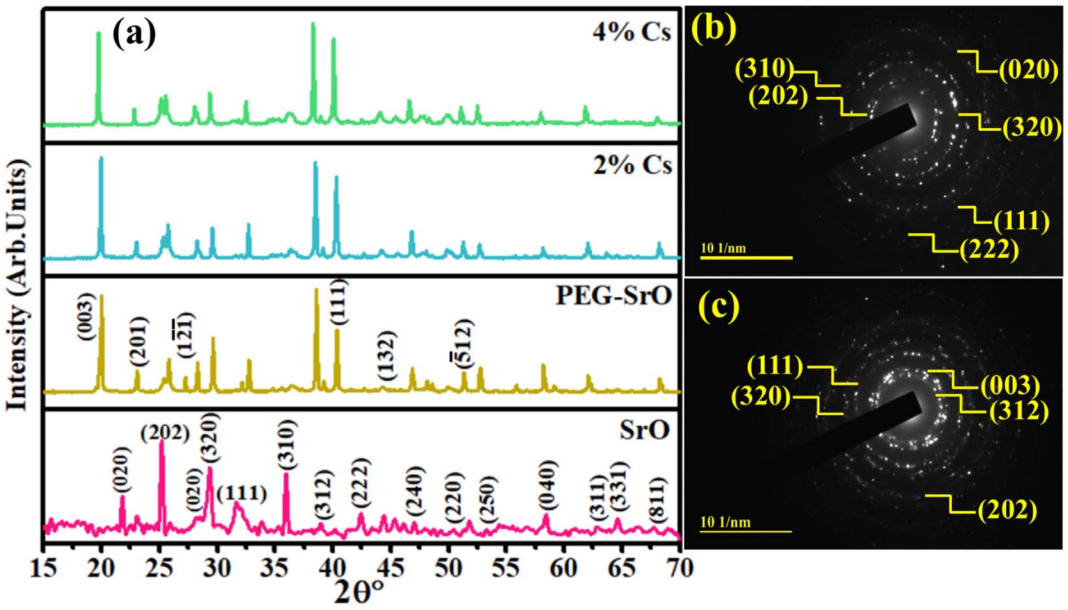

Fig. 2 (a) XRD graph of pure and doped SrO and (b and c) SAED images of pure[11] and 4% Cs/PEG-SrO.

respectively (JCPDS card no. 96-101-0385). Furthermore, diffraction peaks appeared at 42.43° and 44.55°, which are attributed to the (222) and (132) planes of monoclinic $SrO_2(H_2O_2)_2$, respectively (JCPDS card no. 01-073-2209). The peaks observed at 29.37°, 51.7°, 53.22°, and 67.77° are associated with the (320), (5̄12), (250), and (811) planes related to the

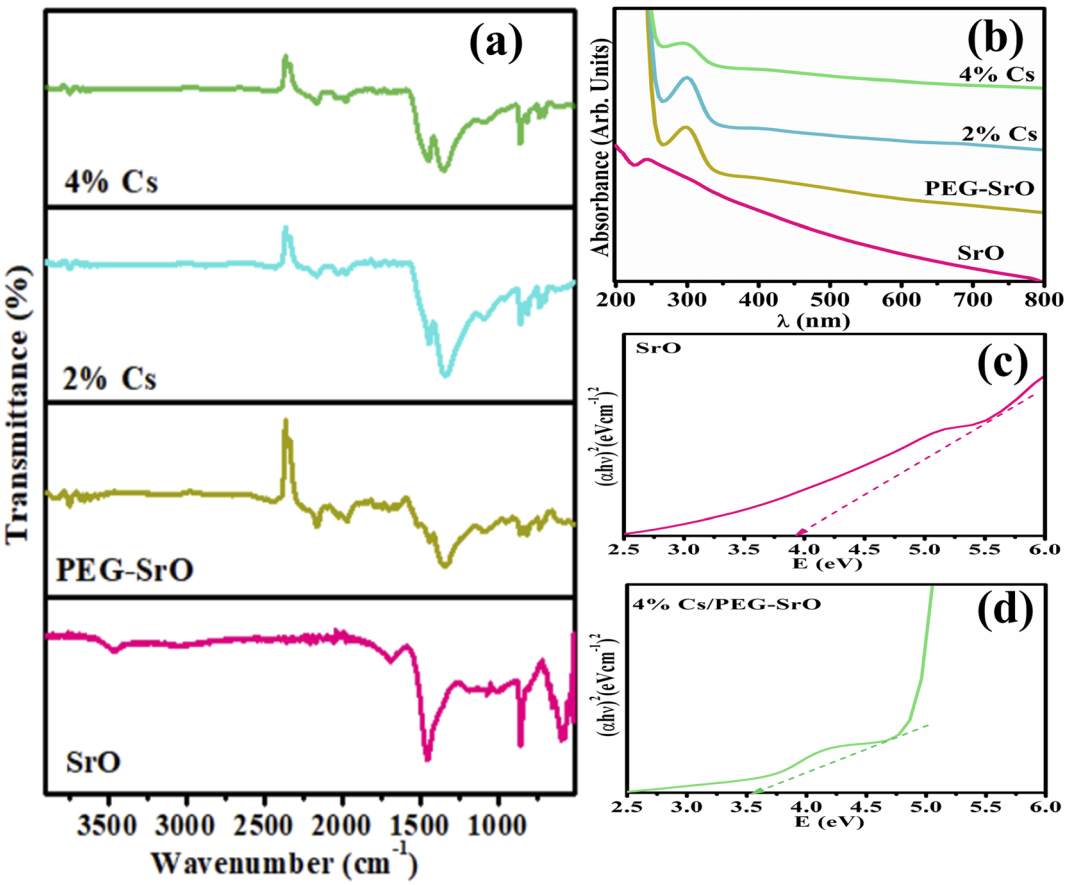

Fig. 3 (a) FTIR and (b) UV-vis spectra and (c and d) Tauc plots of SrO, and 4 wt% of Cs/PEG-SrO.

tetragonal geometry of $Sr(NO_2)_2 \cdot H_2O$, respectively (JCPDS card no. 01-077-0343). The diffraction peak at 21.76° (020) corresponds to orthorhombic $Sr_2(NO)_2$ (JCPDS card no. 00-037-0506). Upon incorporating PEG, additional peaks emerged at 20.07° and 27.28°, corresponding to the (003) and $(1\bar{2}\bar{1})$ crystal planes of $Sr_2O_{28}H_{28}C_{24}$ (JCPDS card no. 96-223-2849). The XRD peaks shifted toward a higher angle,[30] and an increase in intensity was observed, indicating the favorable crystalline properties of PEG.[31] Upon Cs in the binary system, the intensity further increased owing to the enhancement in crystallinity. Moreover, upon increasing the Cs concentration, the peaks shifted towards a lower diffraction angle, which is attributed to crystal expansion.[32] The measured crystallite size of pure, PEG-SrO, 2 and 4 wt% of Cs/PEG-SrO was found to be 54.66, 62.36, 62.36, and 72.72 nm, respectively as determined by the Debye–Scherrer equation. SAED pattern of the undoped and (4 wt%) Cs/PEG-SrO exhibited bright circular fringes, confirming the polycrystalline nature of the prepared samples, as depicted in Fig. 2b and c, respectively.

FTIR spectra were recorded in the range of 3900 to 510 cm^{-1} to analyze the chemical functional groups present in the samples, as depicted in Fig. 3a. FTIR spectrum of SrO revealed a band at ~592 cm^{-1} related to Sr–O stretching, whereas the bands at 857 cm^{-1} and 1063 cm^{-1} are attributed to the symmetric and asymmetric vibration of the Sr–O bond, respectively.[33,34] Moreover, the bands at 1444 cm^{-1} and ~1700 cm^{-1} are ascribed to the bending vibrations of the O–H groups and C=O bonding, respectively.[35,36] The band at 3462 cm^{-1} represents the –OH group and interstitial water molecules.[37] In the spectrum of the binary system, the characteristic bands of PEG appeared at 955, (–CH out-of-plane bending),[38] 1094 (C–O–C stretching vibration),[39] 1342 (C–H bending vibration),[40] 1966 (C–H stretching vibrations),[41] 2157 (presence of CN groups)[42] and 3749 cm^{-1} (O–H stretching).[43] The FTIR spectra of (2 and 4 wt%) Cs/PEG-SrO exhibited no additional bands.

The optical properties of the prepared SrO, PEG-SrO, and (2 and 4 wt%) Cs/PEG doped SrO were examined using UV-vis spectroscopy in the range of 200 to 800 nm, as revealed in Fig. 3b. SrO exhibited absorption within the range of 225–800 nm, highlighting its significant absorption ability.[44,45] The absorption in the UV zone for the pure sample was observed at 243 nm.[46] The addition of PEG and Cs led to an increase in absorption, as depicted in Fig. 3b. The band gap energy (E_g) values for pure and 4% Cs doped PEG-SrO were found to be 3.93, and 3.57 eV, as calculated using the Tauc plot (Fig. 3c and d).[47] Upon doping, the reduction in E_g could be ascribed to surface defects or the formation of extra energy levels within the conduction and valence band regions.[48,49] The small E_g value can facilitate the electron transfer rate, leading to an enhanced catalytic performance.

The morphology of SrO, PEG-SrO, and (2 and 4wt%) Cs/PEG-SrO was investigated by TEM analysis. The pristine sample demonstrated the formation of agglomerated and randomly oriented rectangular-shaped nanorods, as illustrated in Fig. 4a. The hydrogen bonding of water during its synthesis is accountable for its agglomeration.[50] With the addition of PEG, coalesced non-uniform nanorods with a coating of PEG reduced the diameter of the overlapping nanorods, showing a knot-like morphology, as revealed in Fig. 4b. The inclusion of Cs in the binary system resulted in the dispersion and network-like structure of non-uniform nanorods (Fig. 4c and d). HR-TEM

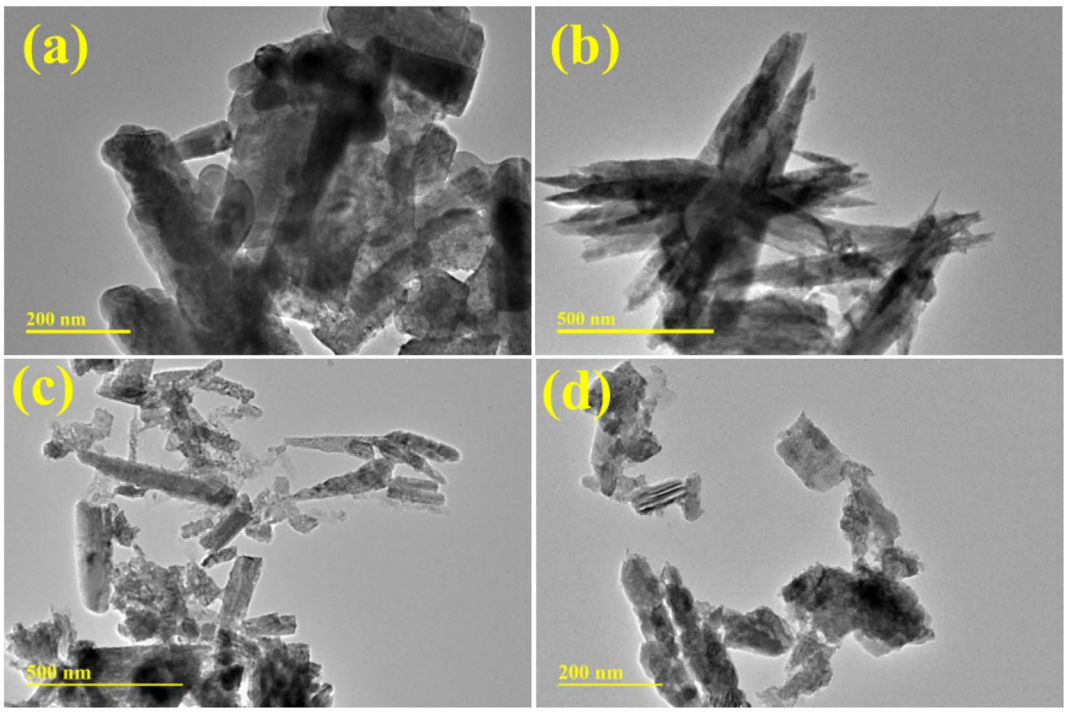

Fig. 4 TEM images (a–d) of SrO,[11] PEG-SrO and (2 and 4 wt%) Cs/PEG-SrO samples.

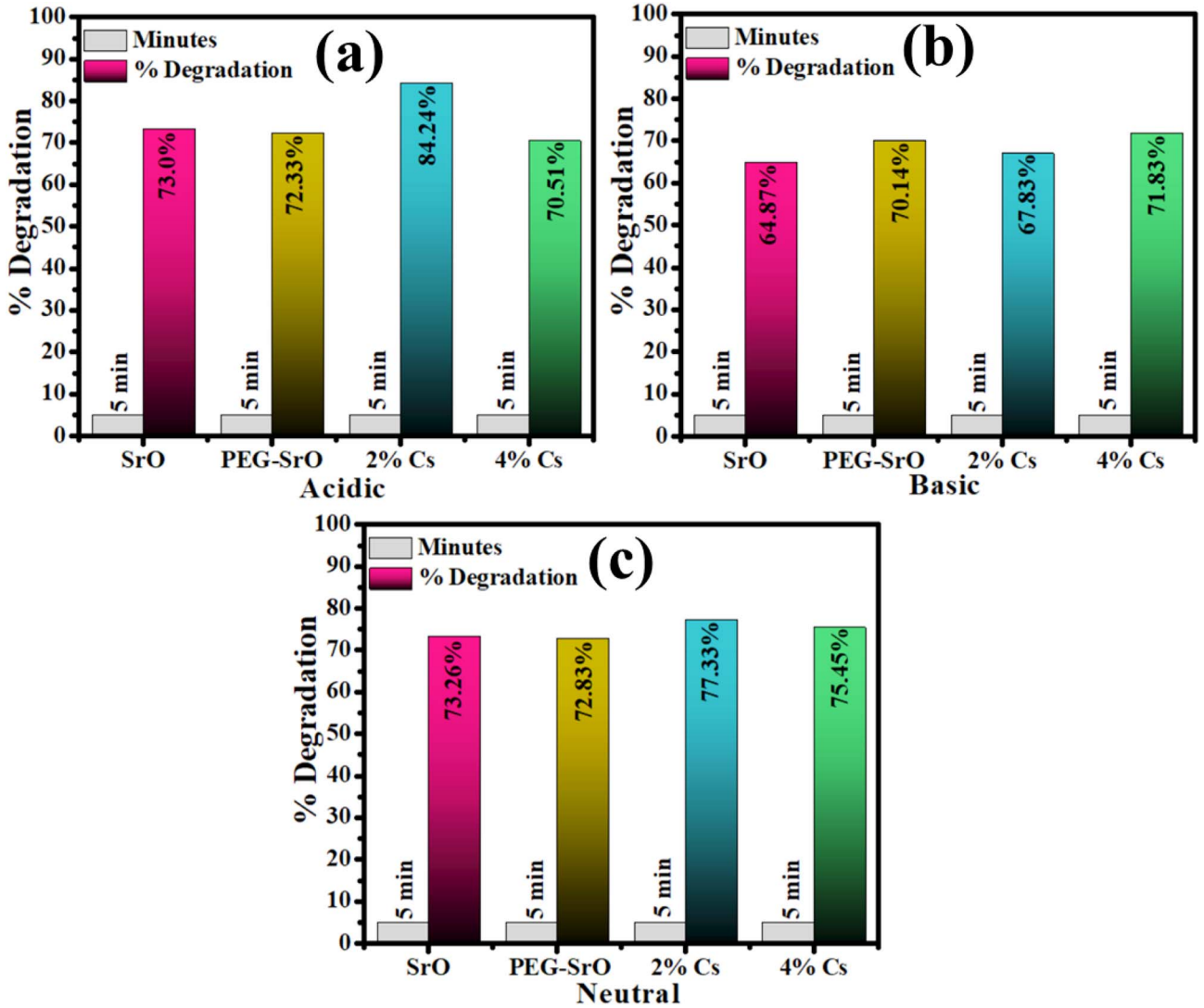

Fig. 5 Catalytic efficiency of SrO and (2 and 4 wt%) Cs/PEG-doped SrO in (a) acidic, (b) basic, and (c) neutral media.

was utilized to determine interplanar *d*-spacing of prepared sample, as shown in Fig. S1. The calculated *d*-spacing values of pure SrO, PEG-SrO and (2 and 4wt%) Cs/PEG-SrO were 0.304, 0.301, 0.303, and 0.304 nm, respectively, which are correlated with the XRD results.

The catalytic mechanism involved a redox reaction where MO served as the oxidizing agent and $NaBH_4$ was utilized as the electron-donating species (Fig. S2). The redox process involved electron transfer from the reducing agent to the MO dye. The incorporation of electrons into the dye promotes the discoloration of MO into its colorless form. The reduction of the dye without a catalyst was a prolonged and less efficient process. The synthesized nanostructures act as an electron relay system, enhancing electron transportation from $NaBH_4$ to the oxidant, ultimately increasing the degradation ability. Both sodium sulfanilate and *N*-dimethyl-*p*-phenylenediamine are by-products resulting from MO.

The catalytic efficiency of pure and doped SrO was evaluated using a UV-vis spectrophotometer in three different media. Fig. 5a–c demonstrate that after a duration of 5 min, the discoloration percentages of MO were approximately 73%, 64.87%, and 73.26% in acidic, basic, and neutral media for the pristine sample, respectively. The degradation rate for the doped samples ranged from 73.0% to 70.51% under acidic conditions, 70.14% to 71.83% under basic conditions, and 72.83% to 75.45% in neutral medium. 2% Cs/PEG-doped SrO

Table 1 Anti-bacterial efficacy of pure and doped SrO

	Inhibition areas (mm)	
Samples	0.5 mg/50 μL	1.0 mg/50 μL
SrO	1.65	2.05
PEG-SrO	2.75	4.55
2% Cs/PEG-SrO	4.15	5.45
4% Cs/PEG-SrO	5.25	6.15
Ciprofloxacin	11.25	11.25
DI water	0	0

exhibited an enhanced catalytic performance in the acidic medium, which is attributed to the generation of H^+ ions upon adding H_2SO_4. The addition of PEG polymer serves as a capping agent to inhibit agglomeration and provide a protective surface layer to control surface defects, thereby improving the degradation efficiency.[51,52] Upon Cs doping, the enhanced catalytic performance could be ascribed to the reduced band gap and increased number of oxygen vacancies.[32] However, 4% Cs/PEG-doped SrO with an increased Cs concentration demonstrated reduced catalytic activity. The negative effect of excessive doping, which is attributed to the large size of alkali cations, may result from the blocking of the active sites.[53]

The antimicrobial efficiency of pure and doped SrO was evaluated using an agar well diffusion method. The inhibition zones ranged from 1.65–5.25 and 2.05–6.15 mm against *E. coli* at low and high concentrations,[11] respectively, as presented in Table 1. Ciprofloxacin served as a positive control, demonstrating a larger inhibition zone (11.25 mm), whereas DI water used as the negative control showed an inhibition zone of 0 mm.

Bactericidal activity is related to the generation of free radicals and reactive oxygen species (ROS) (O^{2-}, OH, HO_2, and H_2O_2),[54] as shown in Fig. S3. The electron-donating properties of MOs generate ROS through different mechanisms, such as

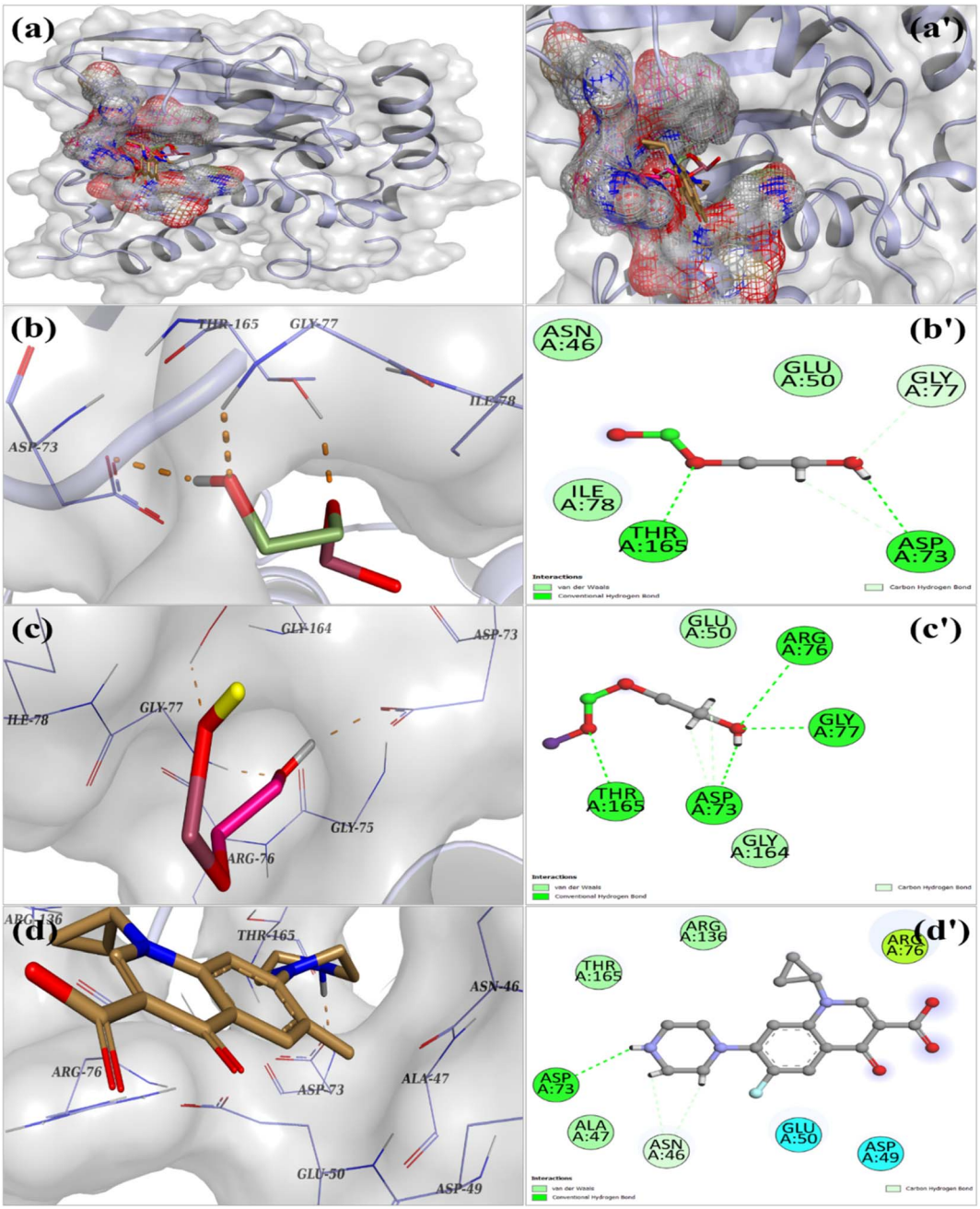

Fig. 6 (a and a′) Ligands binding within DNA gyrase active domain, (b and b′) compound PEG-SrO, (c(3D) and c′(2D)) Cs/PEG-SrO, (d(3D) and d′(2D) ciprofloxacin.

van der Waals forces, hydrophobic interactions, and electrostatic attractions.[55] The positively charged sample interacts with Gram-negative bacteria by electrostatic forces. Due to this interaction, the sample released strontium cations and ROS, destroying the bacterial cell membrane, leading to DNA damage, microbial collapse, and ultimately cell death.[56]

According to the results, 4% Cs/PEG-SrO demonstrated significant antibacterial activity against *E. coli*, Gram-negative bacteria. Upon PEG doping, the long PEG chains enhanced the solubility and provided additional hydroxyl groups on the material surface, improving its bactericidal activity. These hydroxyl groups may also weaken the attachment of extracellular polymeric substances (EPS) to membranes, potentially leading to a detrimental impact on bacterial growth.[43,57] Additionally, when Cs was added, the bacterial growth was inhibited by the electrostatic interactions between Cs^+ and the cell membrane.[58]

3.1. Molecular docking studies

In *silico* exploration provides essential perspectives into ligand–protein interactions, particularly focusing on the bacterial gyrase enzyme, which is a type II topoisomerase that plays a pivotal role in introducing negative supercoils into DNA during protein synthesis. This procedure clarified the mechanisms underlying the anti-bacterial efficacy of Cs/PEG-SrO. The inhibiting agents PEG-SrO, Cs/PEG-SrO, and ciprofloxacin exhibited docking scores (cScores) of 4.03, 4.27, and 5.29, respectively, implying their binding affinities to 5MMN. Fig. 6a and a′ reveal significant conformational alterations within an intricate structure. The ligand-interacting region in PEG-SrO fosters interactions, especially carbon–hydrogen bonds alongside Thr165 and Asp73, and van der Waals interactions with Gly77 (Fig. 6b and b′). Hydrogen bonds are prominently observed with Gly77, Asp73, Thr165, and Arg76 and van der Waals contacts to Gly164 and Glu50 within Cs/PEG-SrO (Fig. 6c and c′). The observed interactions bear a striking resemblance to that of the standard ciprofloxacin within the DNA gyrase-inhibitor complex (Fig. 6d and d′). The correlation between docking affinity and inhibition zones substantiates the conclusion that improved protein binding enhances the antimicrobial efficacy of Cs/PEG-SrO, thereby validating the docking results as a molecular-level explanation for the experimental findings.

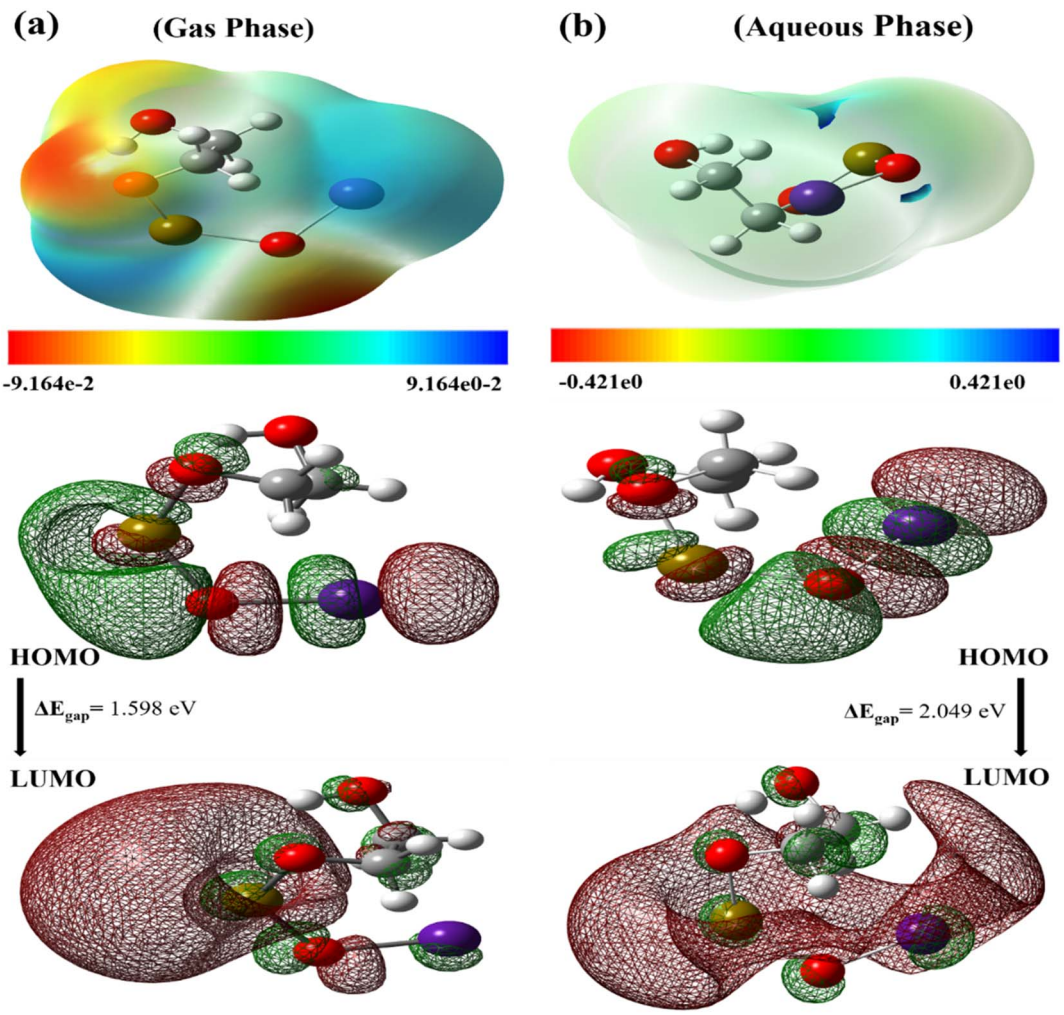

Fig. 7 MESP and HOMO–LUMO analysis of the selected ligand Cs/PEG-SrO, (a) gas phase and (b) aqueous phase.

3.2. DFT and MESP studies

The estimates from density functional theory (DFT) reveal the peculiar electronic properties of the Cs/PEG-SrO composites in both gaseous and aqueous modes (Table S1). A model complex of Cs/PEG-SrO was generated (Fig. S4 and Table S2) and subjected to geometric optimization employing the B3LYP (Becke, 3-parameter, Lee–Yang–Parr) functional alongside the SDD basis set within the Gaussian 09 framework.[59] Aqueous-phase simulations integrated solvation effects *via* the polarizable continuum model (PCM), which conceptualizes the solvent as a continuous polarizable medium. The significant reduction in dipole moment from the gaseous to aqueous phase suggests the crucial role of solvation in maintaining charge distribution and diminishing the average polarity of the molecule. The dielectric shielding influence of solvent stabilizes the electronic levels by reducing electrostatic interactions, clarifying the shift noted in the frontier molecular orbital (FMO) analysis. The deep red regions in the MESP maps, marked by their electronegative potential, highlight areas prone to electrophilic and nucleophilic interactions with molecules, which are crucial for achieving optimal binding (Fig. 7). The Mulliken charges of −1.213584 and −1.361285 for the oxygen atoms in Cs/PEG-SrO indicate the notable existence of negatively charged areas in both phases. Alternatively, green hue suggests neutral areas affecting hydrophobic or van der Waals interactions.

Within the aqueous phase, the heightened degree of chemical hardness signifies improved resistance to electrical deformation and diminished chemical reactivity in polar environments. Solvent molecules create a stabilizing shell that limits the flexibility of the frontier orbitals. The electrophilicity index indicates that the molecule in an aqueous environment demonstrates reduced ability to accept electron density from a nucleophilic perspective. Our findings suggest that aqueous medium contributes to an increase in the thermodynamic stability, decrease in the electrophilic activity, and reduction in the chemical reactivity of Cs/PEG-SrO and these analyzed electronic characteristics, considered as qualitative insights into the local electronic distribution and reactive sites, as vibrational frequency calculations were not carried out. This behavior demonstrates benefits for prospective applications where stability in biological or environmental aqueous systems is essential, encompassing drug delivery, biosensing, or catalytic roles in aqueous environments. Considering all, molecular docking provides the interacting residues of Cs/PEG-SrO in the active site of DNA gyrase, and for the origin of these interactions at the electronic level, DFT calculations highlight charge distribution, electronic polarization, and reactive sites. The distinct electronegative areas and significant negative Mulliken charges concentrated on the oxygen atoms, according to the MESP mapping, are directly linked to the H-bonding and electrostatic interactions identified in docking simulations. This establishes a distinct mechanistic relationship among molecular structure, charge distribution, and biological activity. The observed antibacterial performance is directly attributed to these aspects, as increased surface reactivity and electrostatic interactions facilitate cellular uptake, inhibit enzymes, and ultimately suppress bacterial growth.

4. Conclusion

Strontium oxide (SrO) and SrO doped with PEG and (2 and 4 wt%) Cs were prepared *via* the co-precipitation method. The effectiveness of these materials in degrading methyl orange (MO) dye and their antibacterial activity against *E. coli* were evaluated. The cubic structure of the pure sample was confirmed by the XRD technique, and the measured crystallite size values were 54.66, 62.36, 62.36, and 72.72 nm, respectively. TEM images verified the formation of nanorods of SrO. Furthermore, FTIR spectra revealed the vibrational band of SrO, confirming the successful synthesis of the pure sample. Employing UV-vis spectroscopy, a maximum absorption peak was observed at 243 nm, and a red shift was evident when dopants were introduced. The degradation of MO dye was evaluated using $NaBH_4$ as a reducing agent and the synthesized samples as a catalyst to increase the reaction rate. Among the doped samples, the 2% Cs/PEG-SrO doped specimen possessed the highest dye degradation percentage (84.24%) in acidic medium. The antibacterial studies revealed that (4%) Cs/PEG-SrO exhibited notable bactericidal activity against *E. coli*, with inhibition zones measuring between 1.65–5.25 mm for low concentrations and 2.05–6.15 mm for high concentrations. Moreover, exploring molecular interactions computationally improves nanostructure development for antibacterial applications. In conclusion, (2 and 4 wt%) Cs/PEG-doped SrO are effective catalysts for dye degradation and antibacterial activities, respectively.

Author Contributions

Misbah Tariq – writing original draft, investigation, data curation. Muhammad Imran – conceptualization, supervision, methodology, writing review and editing. Ali Haider – investigation, methodology, writing review and editing. Iram Shahzadi – software, writing original draft, formal analysis (computational study). Fatima Javed – formal analysis, writing original draft, validation. Anwar Ul-Hamid – investigation, resources (morphological analysis). Norah A. Albassami – resources, funding acquisition, writing review and editing. Ghazanfar Nazir – visualization, writing review and editing. Muhammad Ikram – conceptualization, funding acquisition, project administration.

Conflicts of interest

The authors declare that there are no known or potential conflicts of interest related to this study.

Data availability

The data supporting this article have been included as part of the supplementary information (SI). Supplementary information: DFT calculation (quantum chemical descriptors) of specified ligand and coordinates of Cs/PEG-SrO. See DOI: https://doi.org/10.1039/d6ra00841k.

Acknowledgements

Authors are grateful to the Higher Education Commission (HEC), Pakistan, for financial support through NRPU project-20-17615 (PI: Muhammad Ikram). The authors thank the Deanship of Research and Graduate Studies at King Khalid University, Saudi Arabia, for funding this work through the Large Groups Project under Grant Number (RGP2/474/46). First author completed her research work under the supervision of the second author (currently in KFUPM).

References

1 L. S. Maia, L. D. Duizit, F. R. Pinhatio and D. R. Mulinari, Valuation of banana peel waste for producing activated carbon *via* NaOH and pyrolysis for methylene blue removal, *Carbon Lett.*, 2021, **31**(4), 749–762.

2 V. Selvaraj, T. S. Karthika, C. Mansiya and M. Alagar, An over review on recently developed techniques, mechanisms and intermediate involved in the advanced azo dye degradation for industrial applications, *J. Mol. Struct.*, 2021, **1224**, 129195.

3 N. A. Youssef, S. A. Shaban, F. A. Ibrahim and A. S. Mahmoud, Degradation of methyl orange using Fenton catalytic reaction, *Egypt. J. Pet.*, 2016, **25**(3), 317–321.

4 K. Naseem, *et al.*, Investigation of catalytic potential of sodium dodecyl sulfate stabilized silver nanoparticles for the degradation of methyl orange dye, *J. Mol. Struct.*, 2022, **1262**, 132996.

5 N. Zaatout, An overview on mastitis-associated Escherichia coli: pathogenicity, host immunity and the use of alternative therapies, *Microbiol. Res.*, 2022, **256**, 126960.

6 M. K. Elbayoumy, A. M. Allam, A. A. Ghazy and S. M. Nasr, Advances in Controlling Bacterial Mastitis in Dairy Cows, *Egypt. J. Vet. Sci.*, 2024, **55**(1), 1–21.

7 F. S. Hashem and M. S. Amin, Adsorption of methylene blue by activated carbon derived from various fruit peels, *Desalin. Water Treat.*, 2016, **57**(47), 22573–22584.

8 A. B. Dos Santos, F. J. Cervantes and J. B. Van Lier, Review paper on current technologies for decolourisation of textile wastewaters: perspectives for anaerobic biotechnology, *Bioresour. Technol.*, 2007, **98**(12), 2369–2385.

9 S. Zodi, O. Potier, F. Lapicque and J.-P. Leclerc, Treatment of the industrial wastewaters by electrocoagulation: Optimization of coupled electrochemical and sedimentation processes, *Desalination*, 2010, **261**(1–2), 186–190.

10 J. B. Fathima, A. Pugazhendhi, M. Oves and R. Venis, Synthesis of eco-friendly copper nanoparticles for augmentation of catalytic degradation of organic dyes, *J. Mol. Liq.*, 2018, **260**, 1–8.

11 H. Shahzad, *et al.*, Catalytic and antimicrobial properties of Ag and polyacrylic acid doped SrO nanocomposites; molecular docking analysis, *J. Photochem. Photobiol., A*, 2023, **444**, 114970.

12 F. Naz, A. Imran, W. Ullah, K. Saeed, S. Ali and M. N. Khan, Radiation-Induced Degradation of Congo Red Dye over Unsupported and Activated Carbon-Supported Strontium Oxide Nanoparticles, *Iran. J. Chem. Chem. Eng. Res. Artic.*, 2022, **41**(8), 2790–2804.

13 K. B. Kusuma, *et al.*, Synthesis of strontium oxide nanoparticlesby probe sonication method: Its photocatalytic activity and electrochemical sensor studies, *Sens. Int.*, 2023, **4**, 100231.

14 E. O. Naor, M. Koberg and A. Gedanken, Nonaqueous synthesis of SrO nanopowder and SrO/SiO_2 composite and their application for biodiesel production *via* microwave irradiation, *Renewable Energy*, 2017, **101**, 493–499.

15 Y. J. Li, Z. F. Liu, X. P. Liang, J. Ya, T. Cui and Z. C. Liu, Synthesis and electrochromic properties of PEG doped WO3 film, *Mater. Technol.*, 2014, **29**(6), 341–349.

16 T. H. Ho, H. D. Tong and T. T. Trinh, Molecular insights into the interactions between PEG carriers and drug molecules from Celastrus hindsii: a multi-scale simulation study, *Sci. Rep.*, 2024, **14**(1), 16777.

17 M. Ikram, *et al.*, Investigating the catalytic and antibacterial behavior of cesium-doped MoO3 nanostructures against methylene blue dye and MDR E. coli with DFT analysis, *Mater. Today Sustain.*, 2024, **28**, 101031.

18 D. H. Bergey, *Bergey's Manual of Determinative Bacteriology*, Lippincott Williams & Wilkins, 1994.

19 A. W. Bauer, W. M. M. Kirby, J. C. Sherris and M. Turck, Antibiotic susceptibility testing by a standardized single disk method, *Am. J. Clin. Pathol.*, 1966, **45**(4), 493–496.

20 F. Adzitey, *et al.*, Antimicrobial susceptibility and molecular characterization of Escherichia coli recovered from milk and related samples, *Microorganisms*, 2022, **10**(7), 1335.

21 I. I. Lewis and S. James, *Performance Standards for Antimicrobial Susceptibility Testing*, 2022.

22 B. A. Iwalokun, A. Ogunledun, D. O. Ogbolu, S. B. Bamiro and J. Jimi-Omojola, *In vitro* antimicrobial properties of aqueous garlic extract against multidrug-resistant bacteria and Candida species from Nigeria, *J. Med. Food*, 2004, **7**(3), 327–333.

23 P. Rayam, *et al.*, Design and synthesis of oxaprozin-1, 3, 4-oxadiazole hybrids as potential anticancer and antibacterial agents, *J. Heterocycl. Chem.*, 2020, **57**(3), 1071–1082.

24 F. Nazzaro, G. Caliendo, G. Arnesi, A. Veronesi, P. Sarzi and F. Fratianni, Comparative content of some bioactive compounds in two varieties of *Capsicum annuum* L. sweet pepper and evaluation of their antimicrobial and mutagenic activities, *J. Food Biochem.*, 2009, **33**(6), 852–868.

25 A. Haider, *et al.*, Green synthesized phytochemically (*Zingiber officinale* and *Allium sativum*) reduced nickel oxide nanoparticles confirmed bactericidal and catalytic potential, *Nanoscale Res. Lett.*, 2020, **15**, 1–11.

26 I. Shahzadi, *et al.*, Formation of biocompatible MgO/cellulose grafted hydrogel for efficient bactericidal and controlled release of doxorubicin, *Int. J. Biol. Macromol.*, 2022, **220**, 1277–1286.

27 P. Panchaud, *et al.*, Discovery and optimization of isoquinoline ethyl ureas as antibacterial agents, *J. Med. Chem.*, 2017, **60**(9), 3755–3775.

28 J. Shah, H. Sun, Z. Qiao, T. Sharif and M. Gul, Enhanced degradation of methylene blue dye using hydrothermally synthesized Nickel-doped Strontium oxide catalysts, *Brazilian J. Sci.*, 2024, **3**(12), 13–27.
29 M. Kashif, *et al.*, Fe/Ti-codoped strontium oxide nanoparticles for enhanced photocatalytic degradation of methyl orange, *J. Appl. Res. Water Wastewater*, 2024, **11**(1), 8–14.
30 Y. A. Alibwaini, *et al.*, Synthesis, characterizations, optical and photoluminescence properties of polymer blend PVA/PEG films doped eosin Y (EY) dye, *Opt. Mater.*, 2021, **111**, 110600.
31 X. Fu, W. Kong, Y. Zhang, L. Jiang, J. Wang and J. Lei, Novel solid–solid phase change materials with biodegradable trihydroxy surfactants for thermal energy storage, *Rsc Adv.*, 2015, **5**(84), 68881–68889.
32 T. Larbi, M. A. Amara, B. Ouni and M. Amlouk, Enhanced photocatalytic degradation of methylene blue dye under UV-sunlight irradiation by cesium doped chromium oxide thin films, *Mater. Res. Bull.*, 2017, **95**, 152–162.
33 M. D. E. S. Falcão, M. A. S. Garcia, C. V. R. de Moura, S. Nicolodi and E. M. D. E. Moura, Synthesis, characterization and catalytic evaluation of magnetically recoverable SrO/$CoFe_2O_4$ nanocatalyst for biodiesel production from babassu oil transesterification, *J. Brazilian Chem. Soc. São Paulo*, 2018, **29**(4), 845–855.
34 G. Anandhakumari, *et al.*, Synthesis of strontium oxide-zinc oxide nanocomposites by Co-precipitation method and its application for degradation of malachite green dye under direct sunlight, *Heliyon*, 2023, **9**(10), e20824.
35 F. Granados-Correa and J. Bonifacio-Martínez, Combustion synthesis process for the rapid preparation of high-purity SrO powders, *Mater. Sci.*, 2014, **32**, 682–687.
36 A. K. Shimi, *et al.*, Green synthesis of SrO nanoparticles using leaf extract of Albizia julibrissin and its recyclable photocatalytic activity: an eco-friendly approach for treatment of industrial wastewater, *Environ. Sci.: Adv.*, 2022, **1**(5), 849–861.
37 Alimuddin and M. Rafeeq, Synthesis and Characterization of Strontium Oxide Nano Particle by Sol–Gel Method, *Orient. J. Chem.*, 2021, **37**(1), 177–180.
38 G. D. Venkatasubbu, S. Ramasamy, V. Ramakrishnan and J. Kumar, Folate targeted PEGylated titanium dioxide nanoparticles as a nanocarrier for targeted paclitaxel drug delivery, *Adv. Powder Technol.*, 2013, **24**(6), 947–954.
39 A. D. Abreu-Rejón, *et al.*, Effect of PEG grafting density on surface properties of polyurethane substrata and the viability of osteoblast and fibroblast cells, *J. Mater. Sci. Mater. Med.*, 2022, **33**(6), 45.
40 A. León, *et al.*, FTIR and Raman characterization of TiO2 nanoparticles coated with polyethylene glycol as carrier for 2-methoxyestradiol, *Appl. Sci.*, 2017, **7**(1), 49.
41 L. Saravanan and S. Subramanian, Surface chemical studies on the competitive adsorption of poly(ethylene glycol) and ammonium poly (methacrylate) onto alumina, *J. Colloid Interface Sci.*, 2005, **284**(2), 363–377.
42 R. S. A. Sonthanasamy, S. Fazry, B. M. Yamin and A. M. Lazim, Surface functionalization of highly luminescent carbon nanodots from Dioscorea hispida with polyethylene glycol and branched polyethyleneimine and their *in vitro* study, *J. King Saud Univ.*, 2019, **31**(4), 768–779.
43 M. Jayanetti, C. Thambiliyagodage, H. Liyanaarachchi, G. Ekanayake, A. Mendis and L. Usgodaarachchi, In vitro influence of PEG functionalized ZnO–CuO nanocomposites on bacterial growth, *Sci. Rep.*, 2024, **14**(1), 1293.
44 M. M. Hussain, M. M. Rahman and A. M. Asiri, Sensitive L-leucine sensor based on a glassy carbon electrode modified with SrO nanorods, *Microchim. Acta*, 2016, **183**, 3265–3273.
45 G. Anandhakumari, *et al.*, Synergistic effect of strontium oxide–titanium oxide nanocomposites for photocatalytic degradation of malachite green dye, *J. Mater. Sci. Mater. Electron.*, 2024, **35**(26), 1742.
46 A. Kasthuri and P. Pandian, Eco-friendly Synthesis of Strontium Oxide Nanoparticles using Solanum nigrum Leaf Extract: Characterization and Antibacterial Potential, *Orient. J. Chem.*, 2023, **39**(5), 1344–1350.
47 F. El-Sayed, *et al.*, Study of catalytic activity of G-SrO nanoparticles for degradation of cationic and anionic dye and comparative study photocatalytic and electro {\&} photo-electrocatalytic of anionic dye degradation, *J. Mater. Res. Technol.*, 2022, **20**, 959–975.
48 W. Zheng, R. Ding, X. Yan and G. He, PEG induced tunable morphology and band gap of ZnO, *Mater. Lett.*, 2017, **201**, 85–88.
49 A. Rahman, *et al.*, Surface effect of cesium and graphene quantum dots doped CaO to enhance catalytic dye degradation and bacterial inactivation with in-silico analysis, *Surf. Interfaces*, 2025, **56**, 105510.
50 S. Arshad, *et al.*, Evaluation of Bactericidal Potential and Catalytic Dye Degradation of Yttrium/Graphitic Carbon Nitride Doped Nickel Oxide Nanostructures, *J. Inorg. Organomet. Polym. Mater.*, 2024, **34**(5), 2017–2029.
51 R. Soni and M. Navas, ZnO/polyethylene-glycol and ZnO/Au nanocomposites for enhanced photocatalytic degradation of organic dye, *J. Nanoeng. Nanomanuf.*, 2013, **3**(4), 341–347.
52 M. Ikram, *et al.*, Antibacterial potential with evidential molecular docking analysis and catalytic performance of multiple phases AgBr and PVP doped BaO nanorods, *J. Mol. Struct.*, 2025, **1328**, 141371.
53 K. Ciura, G. Grzybek, S. Wójcik, P. Indyka, A. Kotarba and Z. Sojka, Optimization of cesium and potassium promoter loading in alkali-doped $Zn_{0.4}Co_{2.6}O_4|Al_2O_3$ catalysts for N_2O abatement, *React. Kinet., Mech. Catal.*, 2017, **121**, 645–655.
54 E. U. Haq, *et al.*, Catalytic action and bactericidal behavior of samarium/carbon spheres-doped manganese oxide nanostructures and their molecular docking analysis, *J. Alloys Compd.*, 2024, **973**, 172760.
55 M. Z. U. Abidin, *et al.*, Catalytic degradation of methylene blue and bactericidal action by silver and CS-doped iron oxide nanostructures: Experimental and DFT approaches, *Mater. Chem. Phys.*, 2023, **308**, 128300.

56 M. Ikram, *et al.*, Facile synthesis of starch and tellurium doped SrO nanocomposite for catalytic and antibacterial potential: *In silico* molecular docking studies, *Int. J. Biol. Macromol.*, 2022, **221**, 496–507.

57 A. Srisa and N. Harnkarnsujarit, Polyethylene glycol enhanced antibacterial activity of EDTA and ethyl maltol blended PLA against Staphylococcus aureus for biodegradable active packaging, *Food Biosci.*, 2024, **62**, 105237.

58 N. S. Diab, H. M. Ragab, F. A. Hamada, R. A. Aziz, A. M. Alghamdi and M. O. Farea, Influence of cesium bromide nanoparticles on the structural, optical, electrical, and antibacterial properties of polyvinyl alcohol/sodium alginate for biological applications, *J. Vinyl Addit. Technol.*, 2024, **30**(3), 801–813.

59 S. A. Ejaz, *et al.*, *In silico* Investigations of quinine and quinidine as potential Inhibitors of AKR1B1 and AKR1B10: Functional and structural characterization, *PLoS One*, 2022, **17**(10), e0271602.